Advanced interfacial engineering of oxygen-enriched $Fe_xSn_{1-x}OSe$ nanostructures for efficient overall water splitting and flexible zinc-air batteries

Kempanna Harish [a], Jayaraman Balamurugan [b], Thanh Tuan Nguyen [a], Nam Hoon Kim [a,*], Joong Hee Lee [a,c,**]

[a] Advanced Materials Institute of Nano Convergence Engineering (BK21 FOUR), Dept. of Nano Convergence Engineering, Jeonbuk National University, Jeonju, Jeonbuk 54896, Republic of Korea
[b] National Creative Research Initiative Center for Multi-Dimensional Directed Nanoscale Assembly, Department of Materials Science and Engineering, KAIST, Daejeon 34141, Republic of Korea
[c] Carbon Composite Research Centre, Department of Polymer – Nano Science and Technology, Jeonbuk National University, Jeonju, Jeonbuk 54896, Republic of Korea

ARTICLE INFO

ABSTRACT

The rational design of the highly active, durable, and cost-effective catalysts for oxygen reduction reaction (ORR), oxygen evolution reaction (OER), and hydrogen evolution reaction (HER) is essential for next-generation water splitting systems and zinc-air batteries. Herein, a novel strategy is demonstrated to design iron tin oxyselenide ($Fe_xSn_{1-x}OSe$) with enriched oxygen vacancies through a simple and straightforward hydrothermal and subsequent selenization process. The optimal $Fe_{0.33}Sn_{0.67}OSe$ catalyst exhibits superior ORR, OER, and HER performances due to the numerous electroactive sites and high synergistic effects. The water electrolyzer requires a small voltage of 1.490 V and incredible reversibility over 24 h. Most interestingly, the $Fe_{0.33}Sn_{0.67}OSe$ air-cathode based flexible ZAB exhibits a high power density of 153.96 mW cm^{-2} and ultralong cycle life for 400 h. This work opens a new strategy to establish highly active and durable multifunctional catalysts in next-generation energy conversion and storage systems.

1. Introduction

Emerging energy demand and rapid exhaustion of fossil fuels are intensively inspiring the progress in sustainable clean energy storage and conversion technologies [1]. Rechargeable metal-air batteries and water electrolyzers have fascinated numerous interests and are recognized as renewable energy storage and conversion systems [2–4]. Nevertheless, their energy exploitation and power output are seriously hindered by the sluggish electrochemical kinetics of the oxygen reduction reaction (ORR), oxygen evolution reaction (OER), and hydrogen evolution reaction (HER) [5–7]. Noble metals such as Pt, IrO_2, and RuO_2, have been used as highly efficient benchmark catalysts for ORR, HER, and OER [8–10]. However, their high-cost and scarcity nature expressively restrict their large-scale application towards industrial sectors. Therefore, it is essential to design highly active, stable, and cost-effective multifunctional catalysts to enhance the ORR, OER, and HER activities for the scientific interest.

Emerging as a class of cost-effective promising alternatives to existing noble metal catalysts, transition metals and their compounds such as oxides, sulfide, phosphide, and selenide-based catalysts for ORR, OER, and HER [11–13]. In particular, tin selenide ($SnSe_2$) has recently been considered as an electrocatalyst due to its unusual catalytic activities and intrinsic properties [14,15]. However, $SnSe_2$ catalysts suffer from poor cycling durability, which hinders the usage in ORR, OER, and HER activities. Alloying hetero-metal cations is one of the most effective approaches to enhancing catalytic activities and durability to boost the ORR, OER, and HER [16,17]. In addition, the enrichment of oxygen vacancies is another strategy to enhance the electrochemical performance of ORR, OER, and HER [18–20]. The hierarchical design of the three-dimensional (3D) nanoarchitectures with exclusive porous

* Corresponding author.
** Corresponding author at: Advanced Materials Institute of Nano Convergence Engineering (BK21 FOUR), Dept. of Nano Convergence Engineering, Jeonbuk National University, Jeonju, Jeonbuk 54896, Republic of Korea.
 E-mail addresses: nhk@jbnu.ac.kr (N.H. Kim), jhl@jbnu.ac.kr (J.H. Lee).

networks could enhance the electrons/ions transportation kinetics and increase electroactive sites [21,22]. For instance, bimetallic oxyselenide with attractive nanostructures delivered exceptional OER activities with superior durability [23,24]. The splitting of water to engender H_2 and O_2 is a potential aspect for renewable and clean hydrogen energy sources [25–27]. It is essential to develop a new type of catalyst that could reduce the required voltage of water electrolyzes and be suitable for high performance Zn–air batteries [28,29]. Therefore, developing highly effective and durable multifunctional catalysts for water splitting and Zn-air batteries with ultralong cycle life is challenging.

Herein, we describe a novel approach to rational design of iron tin oxyselenide ($Fe_xSn_{1-x}OSe$) nanoarchitectures with enriched oxygen vacancies through a straightforward and low-cost hydrothermal and subsequent selenization process. There has been no study reported on the free-standing and binder-free $Fe_{0.33}Sn_{0.67}OSe$ nanoarchitectures for ORR, OER, and HER activities to the best of our knowledge. Notably, the optimal $Fe_{0.33}Sn_{0.67}OSe$ catalyst exhibited an outstanding ORR performance with a high half-wave potential ($E_{1/2}$) of ~0.84 V vs. RHE, outperforming conventional Pt/C catalyst ($E_{1/2}$ ~0.82 V). Most importantly, $Fe_{0.33}Sn_{0.67}OSe$ based water splitting device required a cell voltage of ~1.490 V and 1.603 V at the current densities of 10 and 100 mA cm^{-2}, respectively and an ultralong cycle life for 90 h, outstanding performance than Pt/C||RuO$_2$ water splitting device. Remarkably, a $Fe_{0.33}Sn_{0.67}OSe$ air-cathode based quasi-solid state rechargeable Zn-air battery (QSS-R-ZAB) delivers a high open-circuit voltage (OCV) of 1.44 V, an ultrahigh specific capacity of ~661.73 mA h g_{Zn}^{-1}, an exceptional peak power density of ~153.96 mW cm^{-2}, and remarkable cycle life for more than 400 h. The QSS-R-ZAB exhibits excellent mechanical durability of more than 10 h at different bending circumstances. Self-driven water splitting powered by a series-connected QSS-R-ZAB device, demonstrating its practical applicability. This present investigation provides a novel approach to design mixed metal oxyselenide-based nanostructures for next-generation water splitting systems and Zn-air batteries, and other renewable energy convergence and storage systems.

2. Experimental section

2.1. Rational design of $Fe_xSn_{1-x}OSe$ nanostructures

All the chemicals and reagents were purchased from Merck and used them without any further purification. The substrate with 2 cm × 5 cm nickel foam (NF) were washed with 3 M HCl, deionized water, ethanol, and acetone for 15 min each to remove the unwanted impurities and oxide layer. In a typical procedure, iron chloride hexahydrate (FeCl$_3$·6H$_2$O; 1.33 mmol), tin chloride dihydrate (SnCl$_2$·2H$_2$O; 2.67 mmol), urea (NH$_2$CONH$_2$, 20 mmol), and ammonium fluoride (NH$_4$F; 12. mmol) were mixed in 50 mL of DI water and continuously stirred it at room temperature until the solution get clear. The as-obtained mixture was then shifted to a Teflon autoclave then NF with an upper surface glass slide cover was immersed. The $Fe_{0.33}Sn_{0.67}$ double hydroxide (DH) precursors was obtained by a hydrothermal reaction at 140 °C for 16 h. For the selenization process, with an appropriate amount of NaBH$_4$ and Se powder (0.2 g) were dissolved in 50 mL in DI water, with continuously stirring then the mixture was transferred to a Teflon autoclave with NF supported $Fe_{0.33}Sn_{0.67}$ DH precursors inside, the selenization process was performed at 180 °C for 2 h. The NF supported $Fe_{0.33}Sn_{0.67}OSe$ was turned to black color that was raised with ethanol and water repeatedly and dried it out at 65 °C in an electric oven. The as-obtained catalyst was denoted as $Fe_{0.33}Sn_{0.67}OSe$ nanosheets. For comparison, the $Fe_xSn_{1-x}OSe$ nanostructures catalyst were fabricated with the changing molar ratios of Fe: Sn to be 0:1, 1:1, 2:1, and 1:0 by similar procedure of the $Fe_{0.33}Sn_{0.67}OSe$ nanosheets, resulting electrodes were designated as SnOSe, $Fe_{0.5}Sn_{0.5}OSe$, $Fe_{0.67}Sn_{0.33}OSe$, and FeOSe nanostructures, respectively. The catalysts of mass loadings were about 2.1, 1.8, 2.0, 1.9, and 2.1 mg cm^{-2} for SnOSe, $Fe_{0.33}Sn_{0.67}OSe$,

$Fe_{0.5}Sn_{0.5}OSe$, $Fe_{0.67}Sn_{0.33}OSe$, and FeOSe nanostructures, respectively.

2.2. Characterization techniques

The as-obtained catalysts were measured by morphological studies using TEM (JEM-ARM200F, Japan), and FE-SEM (JEOL JSM-6701F, Japan), in the Center for University-Wide Research Facilities (CURF) at the Jeonbuk National University (JBNU), South Korea. The AFM (XE-100, Park System Co., Korea) for roughness and thickness of the optimal $Fe_{0.33}Sn_{0.67}OSe$ catalyst was investigated. The obtained catalysts were measured of the elemental composition by ICP-OES (J-A1100) and EDX (SUPRA 40 VP: Carl Zeiss, Germany). The crystalline nature of the as-obtained catalysts was examined by powder XRD pattern (Cu Kα radiation, λ = 0.154 nm) at CURF. For BET analysis, the Ni foam supported active catalysts were scraped and used it as powder. The as-obtained catalysts textural properties were measured by BET analysis with a Micromeritics ASAP 2020. The chemical composition and bonding nature of the as-obtained catalysts were measured by XPS using a Theta Probe (Thermo Fisher Scientific, USA) in the Jeonju center of KBSI.

2.3. Electrochemical performances

The electrochemical analyses were carried out using an electrochemical workstation CHI 760E (CHI Instruments, USA) using direct grown Ni foam active catalysts as freestanding working electrode, Hg/HgO and carbon rod as the reference electrodes and auxiliary, correspondingly. The potentials were converted into RHE through the equation of $E_{RHE} = E_{Hg/HgO} + 0.059$ pH + $E°_{Hg/HgO}$. The electrochemical performances were conducted at a room temperature of 25 ± 0.2 °C. The Pt/C 20 wt% and RuO$_2$ catalysts were fabricated according to previous report [23]. The active catalysts coated NF were fixed on RDE as working electrode, Hg/HgO and carbon rod employed as reference and auxiliary electrodes, respectively. For comparative studies, a comparable weight of Pt/C and Nafion binder were mixed with 350 μL ethanol, 350 μL of water under ultrasonication for an hour, followed by coating on NF by dropping method. The LSV electrochemical performances were performed in 0.1 M KOH O$_2$ saturated solution at different rotating speeds of 400–2800 rpm. During the ORR performance, the continuous O$_2$ flow was maintained. The chronoamperometry test was carried out for the ORR stability with a constant voltage to be −0.3 V vs. Hg/HgO. For OER and HER performance the LSV was investigated with a fixed sweep rate of 1 mV s^{-1}. To examine the resistance of all catalysts, the EIS studies was carried out at the frequency range of 10^6 Hz to 0.1 Hz. The ECSA of the catalysts was measured in the non-faradaic potential region at various sweep rate from 10 to 100 mV s^{-1} to measure the C$_{dl}$. The electroactive materials of the reactive surface area were derived from the C$_{dl}$ value.

2.4. Fabrication of quasi solid-state Zn-air batteries

Quasi solid-state ZAB was assembled with, Zn foil (thickness ~0.25 mm) as the anode, PVA hydrogel film containing 6.0 M KOH and 0.02 M Zn(ac)$_2$ as the gel-electrolyte and the NF supported $Fe_{0.33}Sn_{0.67}OSe$ catalyst as the freestanding air-cathode. These air-cathode, PVA hydrogel, and Zn foil were assembled and a pressure of 3 MPa was applied for 300 s with a pressing roll to enhance the QSS-R-ZAB device integrity.

3. Results and discussion

3.1. Materials characterization

The fabrication process and rational design of the $Fe_xSn_{1-x}OSe$ nanostructures series is schematically presented in Scheme 1. First, we prepared Fe_xSn_{1-x} double hydroxide (DH) precursors by a facile and cost-effective hydrothermal method. Then, we carried out controlled-
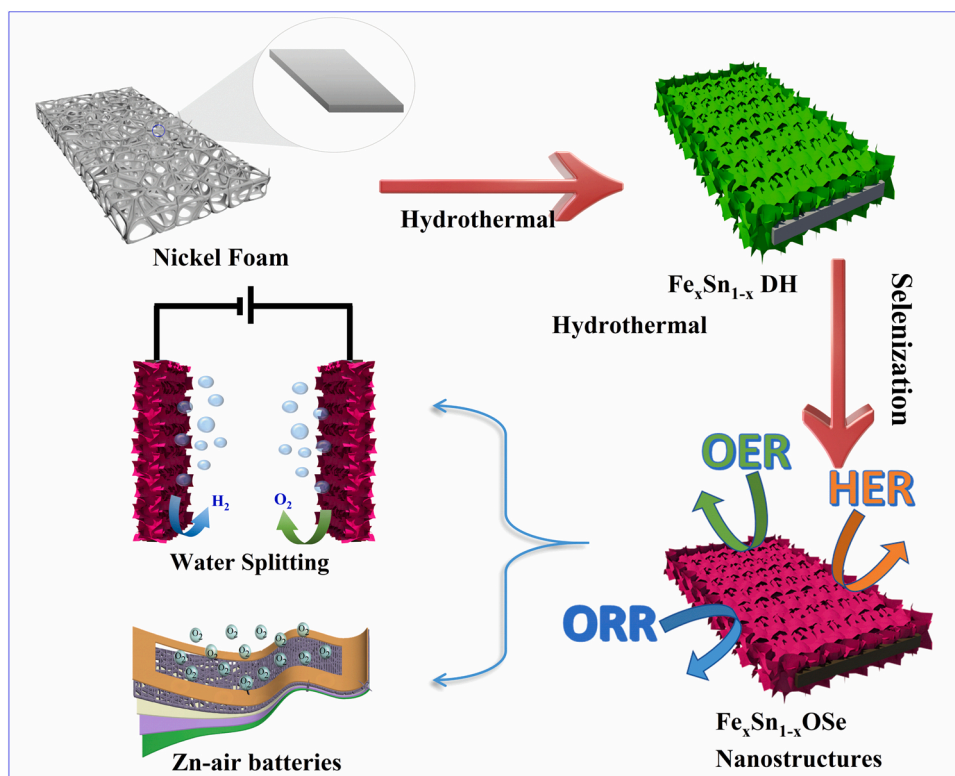
Scheme 1. Schematic illustration for the fabrication of $Fe_xSn_{1-x}OSe$ nanostructures and their applications in water splitting systems and QSS-R-ZAB batteries.

selenization approach for the effective convert to metal-selenide and developed the numerous oxygen vacancies throughout the nanosheet arrays. In order to achieve the oxygen vacancies, we tuned the mass ratio of Fe_xSn_{1-x} DH precursors and selenium sources. The field emission scanning electron microscopic (FE-SEM) images of the $Fe_xSn_{1-x}OSe$ nanostructures are presented in Figs. 1 and S1. In case of pure SnOSe nanostructure, the SEM image clearly shows the different sizes of the nanoparticles are weakly attached over Ni foam (NF), whereas the SnOSe nanostructure displays the different sizes and various thicknesses of the nanosheets grown over the NF, which may reduce the electrolyte ion penetration into the active catalysts and results in poor electrochemical activity and durability. The Fe^{3+} doping into the initial DH precursors may plays a key role in tuning the morphology and enhance the ORR, OER, and HER activities. At the initial precursor ratio of Fe: Sn was to be 1: 2 (i.e., $Fe_{0.33}Sn_{0.67}OSe$), the ultra-thin nanosheet arrays with interconnected nanonetworks were grown on an entirely NF substrate and no noticeable overgrowth was observed (Fig. 1a,b). The atomic force microscopy (AFM) image in Fig. S2 showed that the $Fe_{0.33}Sn_{0.67}OSe$ nanosheets with the thickness around 3.1 nm were perpendicularly grown over NF, representing its hierarchical 3D nanoarchitectures. Such hierarchical nanoarchitectures with unique porous networks which boost the electroactive sites and increase the ion transport kinetics, therefore it leads to increase the ORR, OER, and HER catalytic activities and durability. When the molar ratios of Fe: Sn was to be 1: 1 or higher ($Fe_{0.5}Sn_{0.5}OSe$ or $Fe_{0.67}Sn_{0.33}OSe$), the thickness of the nanosheets significantly increased and we observed there was some aggregation over the NF substrate (Fig. S1b–d). The insertion of Fe^{3+} could confine SnOSe crystal growth along the basal plane, improve the nanosheets quality and lowers the aggregation. The morphological study clearly showed that the optimal Fe to Sn stoichiometric is 1: 2 to attain hierarchical 3D nanosheets with enhanced electrochemical properties. For comparison, the morphological investigation of Fe_xSn_{1-x} hydroxide precursors was studied by SEM and TEM analyses and shown in Fig. S3. The Fe_xSn_{1-x} hydroxide precursor's morphologies were well-matched with the corresponding $Fe_xSn_{1-x}OSe$ nanostructures. This result

reveals that the $Fe_xSn_{1-x}OSe$ holds the nanostructures without any morphological changes during the controlled selenization process. We proved the existence of Fe, Sn, O, and Se elements in the $Fe_{0.33}Sn_{0.67}OSe$ nanosheets by energy dispersive spectroscopy (EDS) characterization (in set of Fig. 1b). The molar ratio of Fe and Sn is nearly 1: 2, which is good consistent with inductively coupled plasma optical emission spectrometry (ICP-OES) results in Table S1. The uniform distribution of the Fe, Sn, O, and Se elements in the $Fe_{0.33}Sn_{0.67}OSe$ nanosheets was further exemplified by SEM–EDS color mapping evaluation (Fig. 1c).

The intrinsic morphology of the $Fe_{0.33}Sn_{0.67}OSe$ nanosheets was further studied by typical transmission electron microscopy (TEM) characterization (Fig. 2). The TEM image in Fig. 2a, shows the thin $Fe_{0.33}Sn_{0.67}OSe$ nanosheets with numerous wrinkled features. Selected-area electron diffraction (SAED) pattern clearly shows the polycrystalline nature of the as-obtained $Fe_{0.33}Sn_{0.67}OSe$ nanosheets (insert of Fig. 2a). The HR-TEM and the corresponding FFT pattern indicates that a highly crystalline $Fe_{0.33}Sn_{0.67}OSe$ nanosheet displays a d-spacing of ~0.293 nm, which relates to the (011) facet of orthorhombic $Fe_{0.33}Sn_{0.67}OSe$ phase (Fig. 2b, inset of Fig. 2b). The morphological investigation and elemental distributions further proved by HAADF-STEM images and EDS mappings in Fig. 2c, which supports the well distribution of the Fe, Sn, O, and Se throughout $Fe_{0.33}Sn_{0.67}OSe$ nanosheets.

Fig. 3a presents the X-ray diffraction (XRD) patterns of the $Fe_xSn_{1-x}OSe$ nanostructures with different Fe: Sn molar ratios. In case of pure SnOSe, the XRD pattern showed the mixture of the benchmark pattern between SnSe and SnO phase (JCPDS no.00-048-1224 and 01-085-0423) [30,31]. The XRD pattern of the SnOSe nanostructure shows five foremost peaks at $2\theta = $ ~18.1, 29.8, 29.9, 33.2, and 50.7°, which are related to the (001), (011), (111), (110), and (121) planes, respectively. At an initial precursor ratio of Fe: Sn of 1: 2 (i.e., $Fe_{0.33}Sn_{0.67}OSe$), the XRD pattern almost similar to that of the pure SnOSe nanostructure. Notably, two additional peaks were observed at 23.7 and 35.2°, which indexed to the cubic FeSe intermediate phase with (JCPDS no.03.-065-9126), demonstrating that the successful formation of the
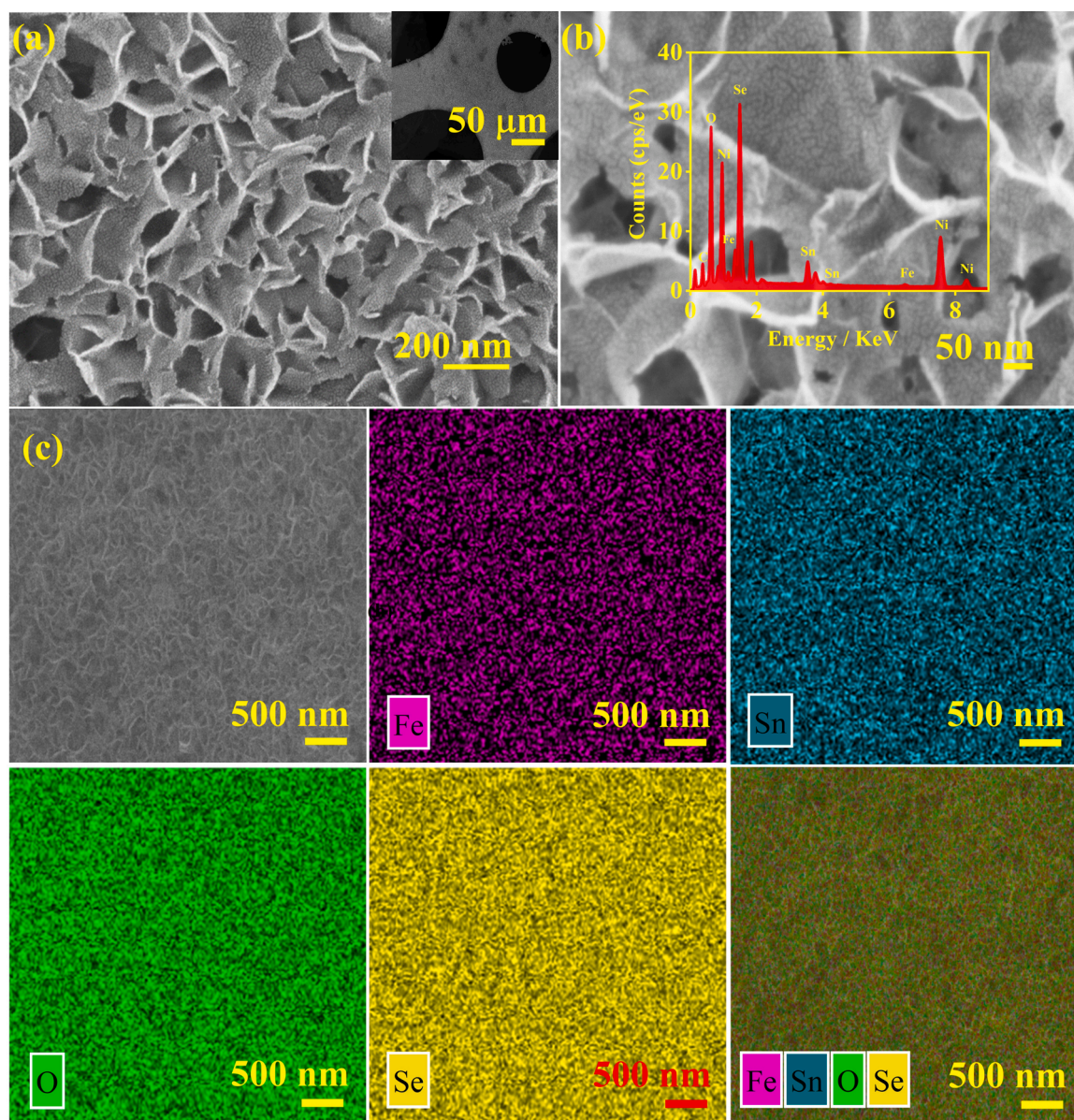
Fig. 1. The morphological investigations of $Fe_{0.33}Sn_{0.67}OSe$ nanostructures: (a) Low, and (b) high-magnification SEM images of the $Fe_{0.33}Sn_{0.67}OSe$ nanosheets, and (c) SEM-EDS color mapping of the $Fe_{0.33}Sn_{0.67}OSe$ nanosheets and their corresponding Fe, Sn, O, Se elements.

alloy structure of $Fe_{0.33}Sn_{0.67}OSe$ nanosheets. With further increase of the molar ratio of Fe: Sn is 1: 1 or higher (i.e., $Fe_{0.5}Sn_{0.5}OSe$ or $Fe_{0.67}Sn_{0.33}OSe$), we observed the orthorhombic and cubic mixture phase formation, indicating the prominent structural transformation from the orthorhombic to the cubic phase [32,33]. For pure FeOSe, the XRD arrangement fully matches with the FeSe cubic phase (JCPDS no.03-065-9126). Most remarkably, the (011) plane in the diffraction peaks steadily shifted toward the lower 2θ angles as the Fe content increased from 29.8 to 29.6°. Furthermore, the diffraction peaks of the (011) plane represents symmetric characteristic and well-ordered. The lattice parameter of the $Fe_xSn_{1-x}OSe$ nanostructures increased gradually from 0.60 to 0.62 Å, which was in well consistent with the (011) plane sequential shift. Vegard's law with their linear trend offered indispensable evidence that Fe^{3+} and Sn^{4+} were successfully integrated into the cubic lattice to obtain the $Fe_xSn_{1-x}OSe$ nanostructure [34,35]. Note that, the close ionic radii of Fe^{3+} (0.58 Å) and Sn^{4+} (0.62 Å), the Fe dopant reinstate the Sn atom from the SnOSe central of octahedron position [36]. In contrast, the XRD patterns of the corresponding Fe_xSn_{1-x} hydroxide precursors are illustrated in Fig. S4.

The elemental compositions and surface electronic structures of the $Fe_{0.33}Sn_{0.67}OSe$ nanosheets were further demonstrated by X-ray photoelectron spectroscopy (XPS) as presented in Fig. 3d–g. The survey XPS spectrum clearly indicates that the presence of elements Fe, Sn, O, and Se in the $Fe_{0.33}Sn_{0.67}OSe$ nanosheets (Fig. S5). As illustrated in Fig. 3d, the deconvoluted Fe $2p_{3/2}$ showed three peaks at ~709.9, 714.5, and 718.5 eV indicated to Fe^{2+}, Fe^{3+}, and supplemented with a satellite peak, which confirms the presence of the Fe in the $Fe_{0.33}Sn_{0.67}OSe$ nanosheets [37,38]. Notably, the Fe 2p peaks in $Fe_{0.33}Sn_{0.67}OSe$ nanosheets displays a positive peak shift of ~0.65 eV when compared to pure FeOSe, representing strong synergetic interaction between Fe and Sn in the $Fe_{0.33}Sn_{0.67}OSe$ nanosheets. The deconvoluted Sn $3d_{5/2}$ displayed two peaks at ~486.67, and 495.25 eV, whereas deconvoluted Sn $3d_{3/2}$ showed peaks at ~486.15, 494.58 eV, and two broad satellite peaks, representing the presence of the Sn^{2+} and Sn^{4+} in the $Fe_{0.33}Sn_{0.67}OSe$ nanosheets (Fig. 3e). Similarly, the Sn 3d peaks in $Fe_{0.33}Sn_{0.67}OSe$ nanosheets displays a positive peak shift of ~0.51 eV when compared to pure SnOSe, representing strong synergetic interaction between the tin and iron phases in the $Fe_{0.33}Sn_{0.67}OSe$ nanosheets. The oxygen vacancies
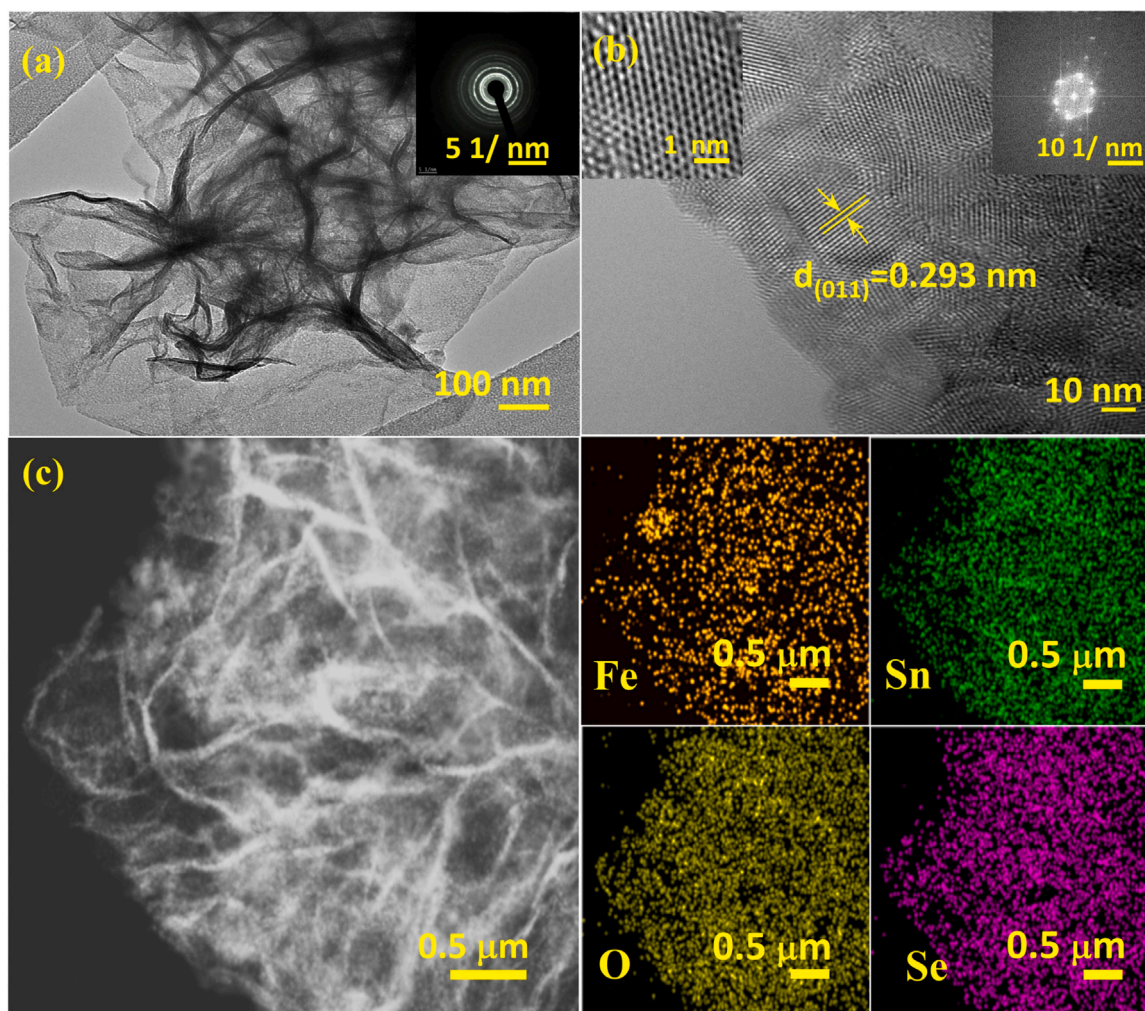
Fig. 2. Morphological investigations of the $Fe_{0.33}Sn_{0.67}OSe$ nanosheets: (a) TEM image (inset show the SAED), (b) HR-TEM image (inset shown the corresponding FFT pattern), and (c) STEM-EDS color mapping of the $Fe_{0.33}Sn_{0.67}OSe$ nanosheets and the corresponding Fe, Sn, O, and Se elements.

confirmed by the O 1 s spectra were measured in the $Fe_{0.33}Sn_{0.67}OSe$ nanosheets. As presented in (Fig. 3f), the main O 1 s spectra of $Fe_{0.33}Sn_{0.67}OSe$ nanosheets are separated to O_I, O_{II}, and O_{III} peaks. The O_I peak positioned at ~529.9 eV is assigned to the M-O bond, the O_{II} peak is situated at ~530.9 eV indicated the developed oxygen vacancy. The O_{III} peak located at ~533.1 eV, which is associated with hydroxyl groups. Moreover, the larger area of O_{II} peak in compared to O_I and O_{III} exhibited in the $Fe_{0.33}Sn_{0.67}OSe$ nanosheets, indicating that during selenium process are controlled by developed of rich oxygen vacancies. As shown in (Fig. 3g), deconvoluted Se 3d revealed three peaks at ~53.8, 55.9, and 58.1 eV, which corresponds to $3d_{5/2}$, $3d_{3/2}$, and SeO_x, respectively [39,40]. The peak located at ~58.1 eV represents the Se-O binding demonstrating the effective formation of iron tin oxy-selenide. For comparison, the XPS analysis of the Fe_xSn_{1-x} hydroxide precursors is presented in Fig. S6.

To comprehend the surface area and pore sizes of hierarchical 3D $Fe_xSn_{1-x}OSe$ nanostructures, we performed the BET analysis. As illustrated in (Fig. S7), the $Fe_xSn_{1-x}OSe$ nanostructures holds a hysteresis loop at the relative pressure (P/P$_o$) of 0.45–1.00, representing the adsorption-desorption of the porous nanoarchitectures. The optimal $Fe_{0.33}Sn_{0.67}OSe$ nanosheets has a larger surface area of ~302 m^2 g^{-1}, which is significantly larger than that of other comparative catalysts such as FeOSe (~185 m^2 g^{-1}), SnOSe (~135 m^2 g^{-1}), $Fe_{0.5}Sn_{0.5}OSe$ (~98 m^2 g^{-1}), and $Fe_{0.67}Sn_{0.33}OSe$ (~225 m^2 g^{-1}). In addition, Barrett-Joyner-Halenda (BJH) pore size distribution reveals the pore diameter

of $Fe_{0.33}Sn_{0.67}OSe$ nanosheets to be around ~3.5 nm. The direct vertical growth hierarchical 3D nanostructures with less structural disorder and unique porosity, which is beneficial to offer a larger surface area. Such hierarchical 3D nanostructures and large surface area of the optimal $Fe_{0.33}Sn_{0.67}OSe$ nanosheets could delivers more electrocatalytic performances for ORR, OER, and HER activities.

3.2. The ORR, OER, and HER performances of $Fe_xSn_{1-x}OSe$ catalysts

The ORR catalytic performance of the as-obtained electrocatalysts were measured in O$_2$ saturated 0.1 M KOH alkaline electrolyte using a three-electrode configuration. At first, we did the typical cyclic voltammetry (CV) analysis in both 0.1 M KOH with O$_2$ and N$_2$-saturated electrolyte at a constant sweep rate of 50 mV s^{-1} was performed, and the results are shown in Fig. S8. The $Fe_{0.33}Sn_{0.67}OSe$ catalyst displayed a featureless CV response in N$_2$-saturated 0.1 M KOH, whereas an apparent cathodic peak appeared at ~0.84 V for O$_2$-saturated 0.1 M KOH, reflecting that tremendous ORR activity.

To further examine the effect of doping the Fe into the $Fe_xSn_{1-x}OSe$ nanostructures, the linear sweep voltammetry (LSV) tests for the as-synthesized catalysts were performed (Fig. 4a). For the comparison, we prepared a conventional Pt/C electrode and analyzed it in a same experimental condition. Consequently, the $Fe_{0.33}Sn_{0.67}OSe$ catalyst exhibited remarkable ORR performance with a higher half-wave potential (E$_{1/2}$) of ~0.84 V and onset potential (E$_{on}$) of ~0.96 V,
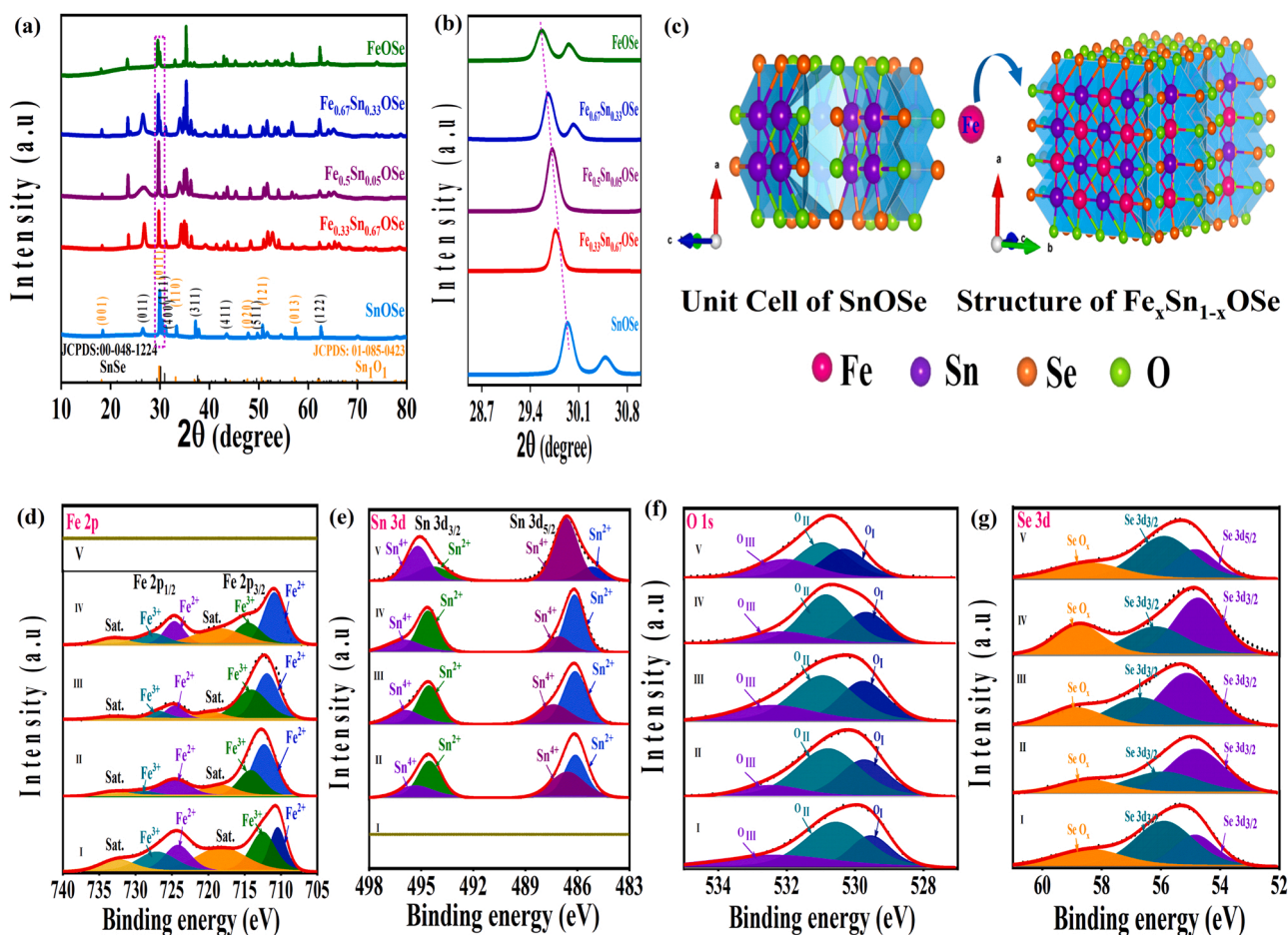
Fig. 3. Structural investigations of the $Fe_xSn_{1-x}OSe$ nanostructures: (a) XRD patterns, (b) XRD patterns zoomed-view of the $Fe_xSn_{1-x}OSe$ nanostructures, (c) $Fe_xSn_{1-x}OSe$ nanostructure formation and the corresponding unit cell of SnOSe crystals, the high-resolution XPS of (d) Fe 2p, (e) Sn 3d, (f) O 1 s, and (g) Se 3d of the $Fe_xSn_{1-x}OSe$ nanostructures: (I) FeOSe, (II) $Fe_{0.67}Sn_{0.33}OSe$, (III) $Fe_{0.50}Sn_{0.50}OSe$, (IV) $Fe_{0.33}Sn_{0.67}OSe$, (V) SnOSe.

outperforming than the benchmark Pt/C ($E_{1/2}$ ~0.83 V; E_{on}~0.99 V) and other counterparts. This result shows that the successful doping of Fe with an optimum ratio can effectively boost the ORR activity. The ORR Tafel slope in (Fig. 4b), represents that the optimal $Fe_{0.33}Sn_{0.67}OSe$ catalyst has a small Tafel slope of ~62 mV dec^{-1}, that is nearby that of Pt/C (~56 mV dec^{-1}) and is much lesser than that of other counterparts, suggesting the excellent ORR kinetics. These results suggest that the ORR activity and kinetics of the $Fe_{0.33}Sn_{0.67}OSe$ catalyst are superior to that of the recently reported state-of-the-art ORR catalysts in the literature (Table S2), demonstrating the good ORR performance till date. The LSVs of the $Fe_{0.33}Sn_{0.67}OSe$ catalyst with various rotational rates from 400 to 2800 rpm, the diffusion-limited current density regularly increases with respect to the rotation speed because the mass transport kinetics increased at higher speeds (Fig. 4c) [41–43].

The Koutecky−Levich (K−L) linearity plots and adjacent concurrence of the fitting lines suggest that the dissolved O_2 concentration and number of electron transfers (n) in the range from 0.25 V to 0.6 V of potential (inset of Fig. 4c). The $Fe_{0.33}Sn_{0.67}OSe$ catalyst has calculated n value of 3.95–3.98, indicating a close-to 4 e$^-$ transfer pathway towards ORR [44,45], which is similar to that of conventional Pt/C (3.95–3.99) (Fig. S9). The rotating ring disk electrode (RRDE) measurement result is in good agreement with the RDE (Fig. S10). Most impressively, the RRDE reveals that the $Fe_{0.33}Sn_{0.67}OSe$ catalyst holds the H_2O_2 yield less than 2% in the potential range between 0.25 and 0.6 V vs. RHE (Fig. S11a). The $Fe_{0.33}Sn_{0.67}OSe$ catalyst showed electron transfer number (n) of 3.86–3.95, which is comparable to conventional Pt/C (n = 3.95–4.00) (Fig. S11b). These results indicate that the

$Fe_{0.33}Sn_{0.67}OSe$ catalyst holds an efficient 4e$^-$ ORR pathway.

Methanol tolerance ability test of the optimal $Fe_{0.33}Sn_{0.67}OSe$ was measured by chronoamperometric analysis in O_2-saturated 0.1 M KOH alkaline electrolyte with fixed potential of 0.55 V (Fig. S12). After methanol injection into the 0.1 M KOH alkaline electrolyte, the $Fe_{0.33}Sn_{0.67}OSe$ catalyst hold the ORR current without noticeable changes, whereas there was significant current density loss for the conventional Pt/C catalyst, which demonstrates that the $Fe_{0.33}Sn_{0.67}OSe$ catalyst exhibits the better ORR selectivity. The $Fe_{0.33}Sn_{0.67}OSe$ catalyst holds current for over 36 h without obvious changes and retained its $E_{1/2}$ value demonstrating outstanding durability (Fig. S13). The morphological characterization further indicates that the $Fe_{0.33}Sn_{0.67}OSe$ catalyst holds its original structure without obvious changes (Fig. S14), further proves its exceptional ORR stability.

The OER activities of the as-obtained catalysts were measured in 1 M KOH alkaline electrolyte using a three-electrode configuration. For comparison, commercial RuO_2 catalyst was coated on NF substrate and employed it as a catalyst. The LSV curves in (Fig. 4d), displays the $Fe_{0.33}Sn_{0.67}OSe$ catalyst highest OER performance, with a small overpotential of ~162 mV at a current density of 10 mA cm^{-2}, superior to that of RuO_2 (~257 mV at current density of 10 mA cm^{-2}), and the optimal ratio of $Fe_{0.33}Sn_{0.67}OSe$ and other comparative all catalysts showed a lower overpotential of current densities of 10 and 100 mA cm^{-2}, respectively (Fig. 4e), much lesser than that of other counterparts and of most of the recently reported state-of-the-art OER catalysts in the literature (Table S3). The $Fe_{0.33}Sn_{0.67}OSe$ catalyst exhibited a low Tafel slope value of ~54.3 mV dec^{-1}, much lower than

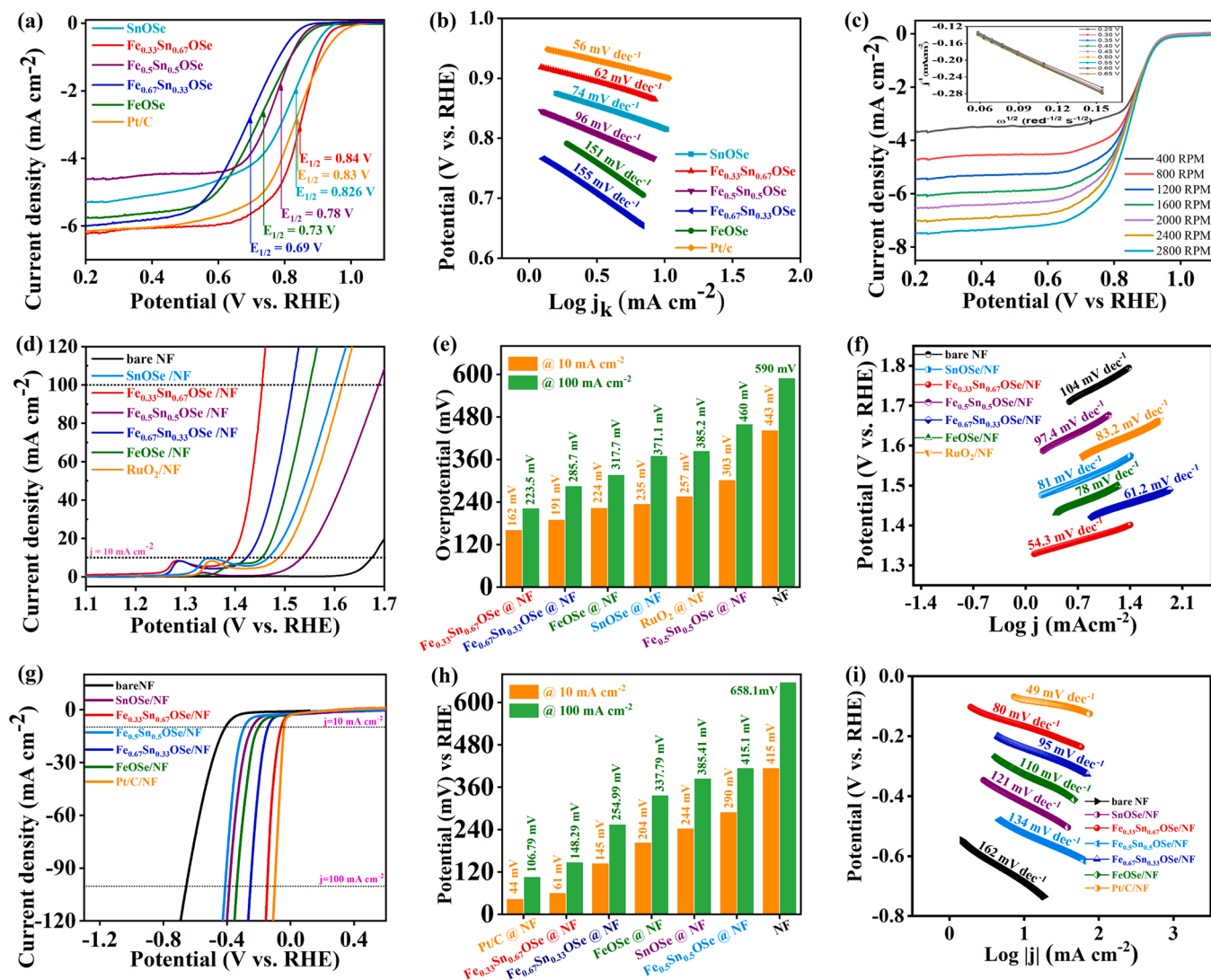**Fig. 4.** Multifunctional activities of the Fe$_x$Sn$_{1-x}$OSe catalysts: (a) The LSV polarization curves of Fe$_x$Sn$_{1-x}$OSe and Pt/C catalysts in O$_2$-saturated 0.1 M KOH electrolyte at the rotation speed of 1600 rpm, (b) the corresponding Tafel plots for ORR, (c) The LSV curves of Fe$_{0.33}$Sn$_{0.67}$OSe catalyst at different rotational speeds from 400 to 2800 rpm, (inset: shows the K−L plots), (d) The LSV polarization curves of Fe$_x$Sn$_{1-x}$OSe and RuO$_2$ catalysts for OER performance in 1.0 M KOH electrolyte at a scan rate of 1 mV s^{-1}, (e) Overpotential of Fe$_x$Sn$_{1-x}$OSe and RuO$_2$ catalysts at a current densities of 10 and 100 mA cm^{-2}, (f) the corresponding Tafel plots for OER(g) The LSV polarization curves of Fe$_x$Sn$_{1-x}$OSe and Pt/C catalysts for HER performance in 1.0 M KOH electrolyte at a scan rate of 1 mV s^{-1}, (h) Overpotential of Fe$_x$Sn$_{1-x}$OSe and Pt/C catalysts at a current densities of 10 and 100 mA cm^{-2}, and (i) the corresponding Tafel plots of Fe$_x$Sn$_{1-x}$OSe catalysts for HER.

conventional RuO$_2$ catalyst (~83.2 mV dec^{-1}) and other comparative catalysts, demonstrating its excellent OER kinetics (Fig. 4f). To examine the electron transport kinetics mechanism during the OER activity, the electrochemical impedance spectra (EIS) measurement as analyzed in the frequency range of 1 MHz- 0.1 Hz at a fixed potential of 1.6 V. Obviously, the Fe$_{0.33}$Sn$_{0.67}$OSe catalyst holds a small charge-transfer resistance (R$_{ct}$) of ~0.62 Ω lower than that of RuO$_2$ (~0.81 Ω) and much lower than that of other counterparts (Fig. S15). To better comprehend the motive behind the exceptional catalytic activities of the Fe$_{0.33}$Sn$_{0.67}$OSe catalyst towards OER, the electrochemically active surface area (ECSA) was attained from the CV curve in the non-Faradaic region and evaluated it by the double-layer capacitance (C$_{dl}$), as presented in (Fig. S16a–f). The Fe$_{0.33}$Sn$_{0.67}$OSe catalyst shows the highest C$_{dl}$ value of ~26.14 mF cm^{-2}, compared to that of other catalysts such as FeOSe (~15.59 mF cm^{-2}), SnOSe (~10.25 mF cm^{-2}), Fe$_{0.5}$Sn$_{0.5}$OSe (~7.97 mF cm^{-2}), and Fe$_{0.67}$Sn$_{0.33}$OSe (~19.54 mF cm^{-2}), indicating the enlargement of electroactive sites in the Fe$_{0.33}$Sn$_{0.67}$OSe catalyst [46].

The Fe$_{0.33}$Sn$_{0.67}$OSe catalyst showed outstanding OER durability with negligible current degradation in chronoamperometric response after 38 h and retained its potential in LSV curves (Fig. S17). The Nyquist plot of the Fe$_{0.33}$Sn$_{0.67}$OSe catalyst after long-term electrochemical stability slightly increased in R$_{ct}$ value of the ~0.68 Ω, further proves its excellent OER durability (Fig. S18). The morphological analysis further indicates that the Fe$_{0.33}$Sn$_{0.67}$OSe catalyst retained their original nanostructure without any loss, indicating its extraordinary electrochemical stability towards OER activity (Fig. S19). The optimal Fe$_{0.33}$Sn$_{0.67}$OSe catalyst exhibits low an OER overpotential, an ultrasmall Tafel slope value, high electroactive surface area, and low R$_{ct}$ compared to those of commercial RuO$_2$ and most reported OER catalysts (Table S3). Therefore, our Fe$_{0.33}$Sn$_{0.67}$OSe stands out as massively an active catalyst for OER. The bifunctional ORR and OER activities further investigated by the value of ΔE [47], which is described as potential difference of both E$_{1/2}$ and E$_{j=10}$ (i.e., ΔE = E$_{j = 10}$ − E$_{1/2}$). The Fe$_{0.33}$Sn$_{0.67}$OSe showed a lower ΔE value of 0.75 V, which is relatively lower than Pt/C−RuO$_2$ couple (ΔE =0.79 V) demonstrating its superior

bifunctional catalytic activities [48,49].

The hydrogen evaluation reaction (HER) activities of the as-obtained catalysts were investigated by LSV in 1 M KOH electrolyte using a three-electrode setup. For comparison, commercial Pt/C was coated on NF substrate and employed it as a catalyst. As shown in Fig. 4g, the $Fe_{0.33}Sn_{0.67}OSe$ catalyst exhibited an excellent HER performance, with an ultralow overpotential of ~61 mV at a current density of 10 mA cm^{-2}, which is close to that of Pt/C (~44 mV at current density of 10 mA cm^{-2}). The optimum ratio of $Fe_{0.33}Sn_{0.67}OSe$ and other all comparative catalysts showed a lower overpotential at current density of 10 and 100 mA cm^{-2}, respectively (Fig. 4h), which is higher than that of other counterparts and most reported HER electrocatalysts (Table S4). The Tafel slope value of the $Fe_{0.33}Sn_{0.67}OSe$ catalyst was about 80 mV dec^{-1}, which is compatible with conventional Pt/C (~49 mV dec^{-1}) and much lower than other counterparts, indicating its tremendous HER kinetics(Fig. 4i). The HER process of the $Fe_{0.33}Sn_{0.67}OSe$ catalyst obeys the Volmer-Heyrovsky mechanism, which is consistent with the

previous report [50,51]. Noticeably, the $Fe_{0.33}Sn_{0.67}OSe$ catalyst possess ultralow R_{ct} of ~0.45 Ω, much lower than Pt/C (~0.71 Ω) and other counterparts (Fig. S20). The $Fe_{0.33}Sn_{0.67}OSe$ catalyst also has a C_{dl} value of ~52.89 mF cm^{-2}, higher than other counterparts of FeOSe (~32.71 mF cm^{-2}), SnOSe (~24.66 mF cm^{-2}), $Fe_{0.5}Sn_{0.5}OSe$ (~12.53 mF cm^{-2}), and $Fe_{0.67}Sn_{0.33}OSe$ (~36.79 mF cm^{-2}), representing its exceptional electroactive sites (Fig. S21a–f). In addition, the $Fe_{0.33}Sn_{0.67}OSe$ catalyst has exceptional electrochemical durability for HER with an insignificant change in potential at a constant current of 100 mA cm^{-2} (Fig. S22a). The LSV curves before and after continuously operating for 38 h was shown in Fig. S22b illustrating the high durability of $Fe_{0.33}Sn_{0.67}OSe$ catalyst for HER. The Nyquist plot clearly indicates that the $Fe_{0.33}Sn_{0.67}OSe$ catalyst with minimum increment in R_{ct} value of ~0.51 Ω after long-term prolonged cycling test, demonstrates its excellent HER durability (Fig. S23). The morphological analysis of the $Fe_{0.33}Sn_{0.67}OSe$ nanosheets were preserved its morphology without noticeable change, further proves its outstanding HER durability (Fig. S24).
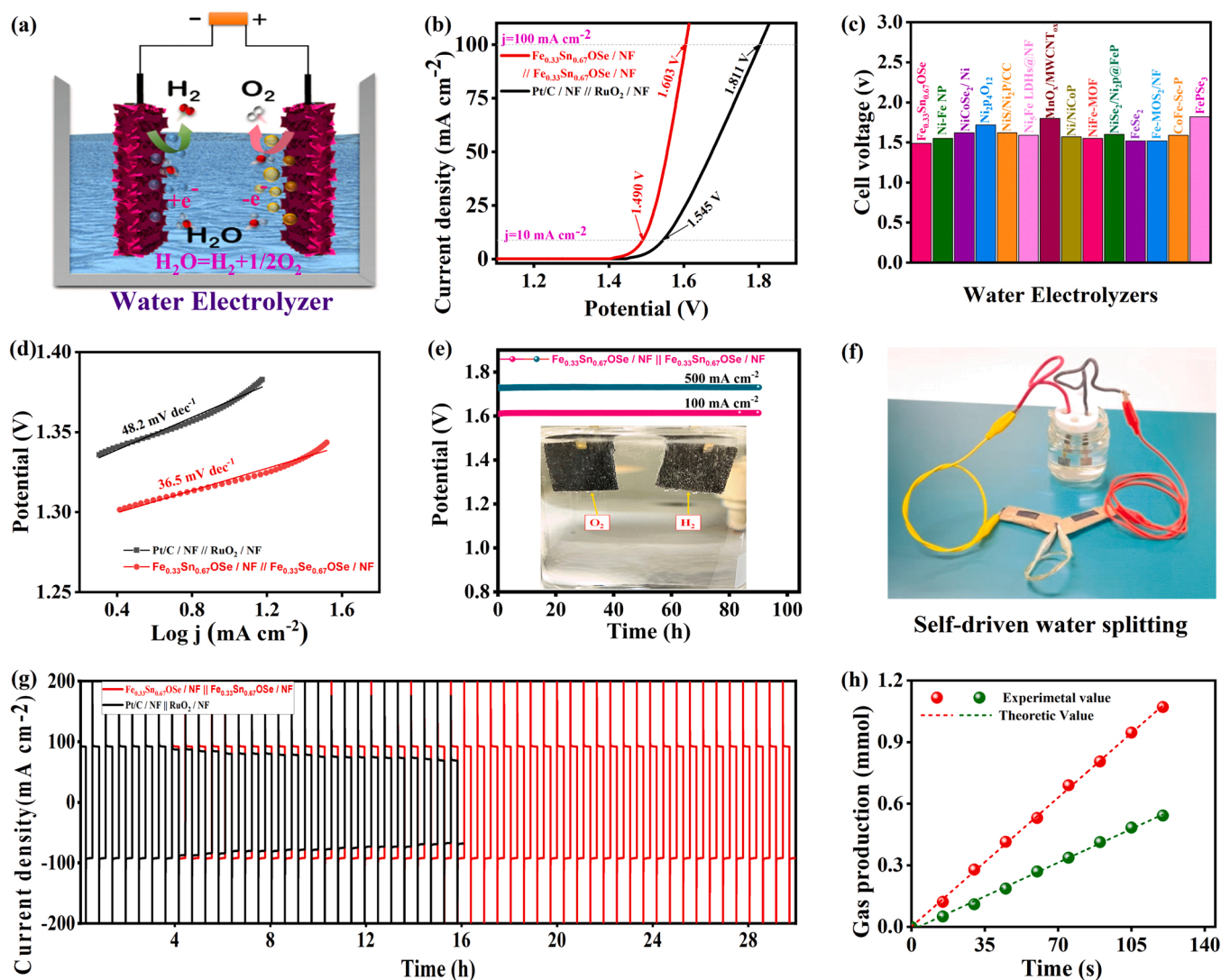

Fig. 5. Electrochemical performance of $Fe_{0.33}Sn_{0.67}OSe$ bifunctional catalyst for overall water splitting: (a) Schematic illustration of alkaline water electrolyzer with $Fe_{0.33}Sn_{0.67}OSe$ bifunctional catalyst, (b) LSV polarization curves of the $Fe_{0.33}Sn_{0.67}OSe||Fe_{0.33}Sn_{0.67}OSe$ and Pt/C||RuO$_2$ water electrolyzer, (c) The cell voltage comparison of $Fe_{0.33}Sn_{0.67}OSe||Fe_{0.33}Sn_{0.67}OSe$ and recent reported electrolyzer @10 mA cm^{-2} in the literature, (d) The Tafel plot for $Fe_{0.33}Sn_{0.67}OSe||Fe_{0.33}Sn_{0.67}OSe$ and Pt/C||RuO$_2$ water electrolyzer, (e) Long-term stability for a $Fe_{0.33}Sn_{0.67}OSe||Fe_{0.33}Sn_{0.67}OSe$ water electrolyzer at a current density of 100 mA cm^{-2} over 90 h (inset show the digital photograph of the water electrolyzer with the generation of O$_2$ and H$_2$ gases), (f) The self-driven water electrolyzer by our series-connected QSS-R-ZABs, (g) The chronoamperometric curve of $Fe_{0.33}Sn_{0.67}OSe||Fe_{0.33}Sn_{0.67}OSe$ water electrolyzer (the polarity reversed every 1000 s), (h) Quantity of H$_2$ and O$_2$ produced by the water electrolyzer system at room temperature, the generated gases were reported has experimentally and theoretically with an interval time.

3.3. The performances of overall water splitting and Zn-air battery

Such promising bifunctional OER and HER performances, we constructed a water splitting cell using the optimal $Fe_{0.33}Sn_{0.67}OSe$ catalyst in the two-electrode system as both anode and cathode in 1 M KOH electrolyte (Fig. 5a). Our water electrolyzers required a small cell voltage of 1.490 V to provide a current density of 10 mA cm^{-2}, outperforming than the Pt/C||RuO$_2$ water splitting cell (1.545 V at current density of 10 mA cm^{-2}) superior to other equivalents and of the most reported water splitting catalysts (Fig. 5b,c). The catalyst exhibits a low Tafel slope of ~36.5 mV dec^{-1}, which is much lesser than that of Pt/C|| RuO$_2$ (~48.2 mV dec^{-1}) (Fig. 5d). As anticipated, our $Fe_{0.33}Sn_{0.67}OSe$|| $Fe_{0.33}Sn_{0.67}OSe$ electrolyzers exhibited superior electrochemical durability with slightly decreased over 90 h in a chronoamperometric test, whereas major current density loss for conventional Pt/C||RuO$_2$ water electrolyzer cells, suggesting that the $Fe_{0.33}Sn_{0.67}OSe$ catalyst is promising for industrial water electrolyzers (Fig. 5e). Apart from the water-

splitting cell stability, to prove the durability of catalyst towards OER and HER reversible activity rarely studied. Therefore, the highly reversible electrocatalyst for water splitting is essential to develop. In earlier reports exhibits, the reversibility analysis carried out at the potential of − 1.603 to + 1.603 V for each 1000 s (Fig. 5g). The $Fe_{0.33}Sn_{0.67}OSe$||$Fe_{0.33}Sn_{0.67}OSe$ device retained without any changes for both OER and HER showed a high current density of 100 mA cm^{-2} for over 30 h. In contrast, the Pt/C||RuO$_2$ water splitting device has decreased by ~56.8% after 16 h, which confirms that our $Fe_{0.33}Sn_{0.67}OSe$||$Fe_{0.33}Sn_{0.67}OSe$ device shows excellent reversibility. Even at a very high current density of 500 mA cm^{-2}, the $Fe_{0.33}Sn_{0.67}OSe$||$Fe_{0.33}Sn_{0.67}OSe$ water electrolyzer exhibited a negligible degradation of current over 90.h, demonstrating that our catalyst potential for industrial sectors (Fig. 5e). To measure the Faradaic efficiency, we calculated the total quantity of O$_2$ and H$_2$ molecules as illustrated in Fig. 5h. We have assembled a homemade water electrolyzer to determine the H$_2$ and O$_2$ evolution during the overall water splitting process (Fig. S25). The calculated O$_2$
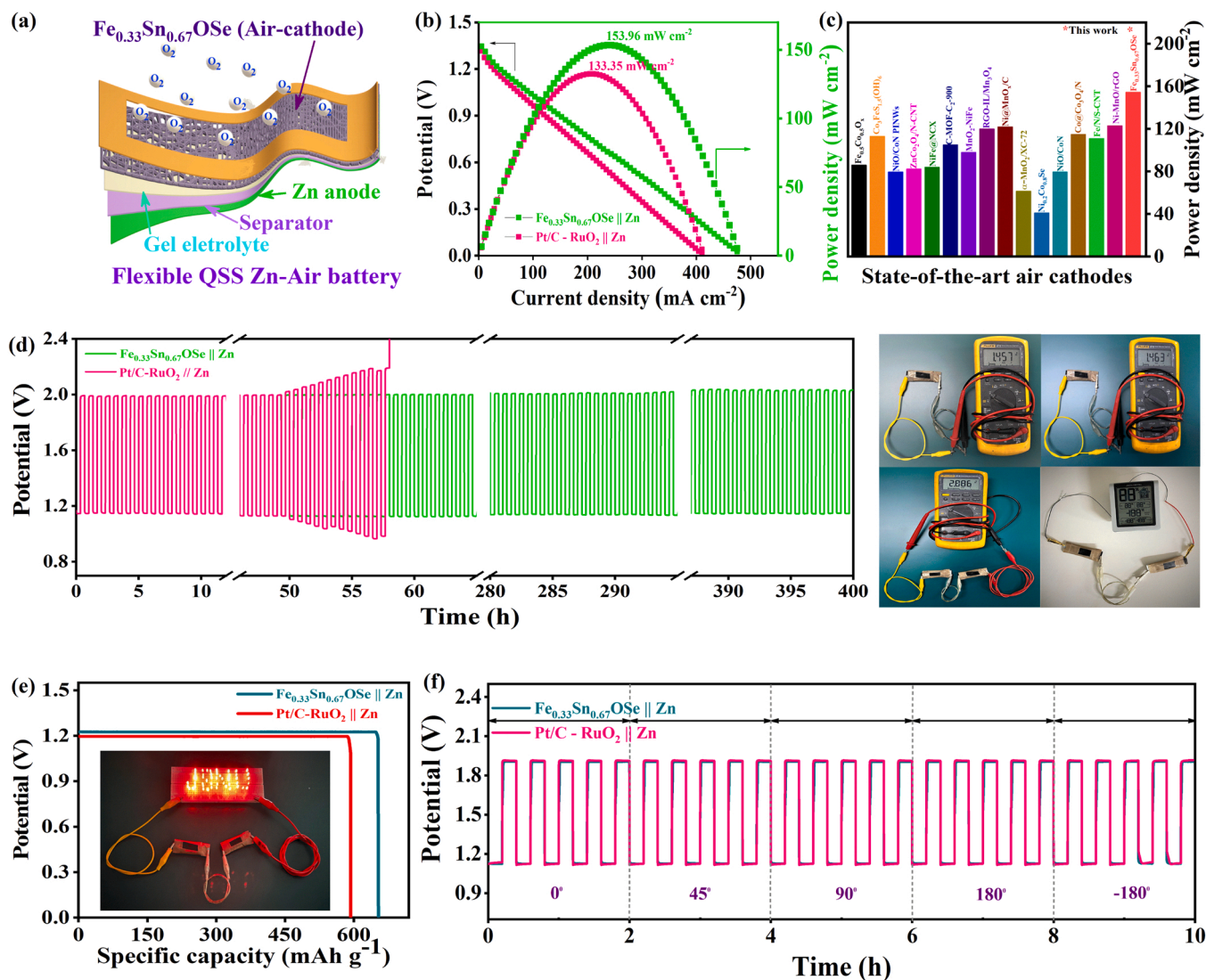
Fig. 6. The flexible QSS-R-ZABs electrochemical performances: (a) Schematic illustration the fabrication of flexible QSS-R-ZAB with the $Fe_{0.33}Sn_{0.67}OSe$ air-cathode, (b) Discharge polarization curves and the corresponding power density plots of the $Fe_{0.33}Sn_{0.67}OSe$ and Pt/C-RuO$_2$ air-cathodes based QSS-R-ZAB, (c) The power density comparison of $Fe_{0.33}Sn_{0.67}OSe$ air-cathodes based QSS-R-ZAB and the state-of-the-art air-cathodes based ZAB in the reported literature, (d) Galvanostatic long-term cycling performance charge-discharge of $Fe_{0.33}Sn_{0.67}OSe$ air-cathode based QSS-R-ZAB with 30 min charging and 30 min discharging at a current density of 10 mA cm^{-2}, (e) The open circuit voltage for flexible $Fe_{0.33}Sn_{0.67}OSe$ air-cathode based QSS-R-ZAB, (f) The specific capacity of $Fe_{0.33}Sn_{0.67}OSe$ and Pt/C-RuO$_2$ air-cathodes based rechargeable QSS-R-ZABs at a current density of 10 mA cm^{-2} f (inset show a photograph of series-connected QSS-R-ZABs powered 51 red LEDs), and (g) The long-term stability and charge-discharge curves of the $Fe_{0.33}Sn_{0.67}OSe$ air-cathode based QSS-R-ZAB at a current density of 10 mA cm^{-2} under different bending circumstances.

and H_2 molar ratios were about 1:2, very close to the theoretical value. The estimated Faradaic efficiency of the $Fe_{0.33}Sn_{0.67}OSe$ catalyst was 98.42% for O_2 production and 98.15% for H_2 production. Therefore, the $Fe_{0.33}Sn_{0.67}OSe||Fe_{0.33}Sn_{0.67}OSe$ device demonstrated overall water splitting with excellent bifunctional OER and HER activities and ultra-long cycle life. Such superior water splitting performance of $Fe_{0.33}Sn_{0.67}OSe$ could be the 3D nanoarchitectures, unique porous framework, high electroactive surface area, and high synergistic effects. To realize the durable nature of the $Fe_{0.33}Sn_{0.67}OSe$ catalyst, the post-treated catalysts was examined by morphological and structural studies. The SEM and TEM images of both post-OER and post-HER side electrodes in overall water splitting retained their original structure without obvious changes, demonstrating the outstanding electrochemical stability (Fig. S26). Moreover, the XRD and XPS were performed to further verify the working ability of $Fe_{0.33}Sn_{0.67}OSe$ catalyst under long-term operation. After HER, OER, and ORR performance, the XRD pattern of $Fe_{0.33}Sn_{0.67}OSe$ catalyst exhibited almost same crystalline structure (Fig. S27), demonstrating possibility for using in long-term condition. Some small additional peaks were appeared after OER, illustrating the partial oxidation of $Fe_{0.33}Sn_{0.67}OSe$ catalyst during OER process. The XPS in Fig. S28 showed the negligible change after stability for ORR, HER, and OER performance, further confirming the outstanding stability of the catalyst.

The quasi-solid state rechargeable Zn-air battery (QSS-R-ZABs) was assembled with NF supported $Fe_{0.33}Sn_{0.67}OSe$ nanosheets, Zn plate, and 6.0 M KOH electrolyte containing 0.2 M $Zn(ac)_2$ as the freestanding air-cathode, anode, and PVA-KOH as the gel electrolyte, respectively (Fig. 6a). The $Fe_{0.33}Sn_{0.67}OSe$ air-cathode based QSS-R-ZAB delivers an ultrahigh open circuit voltage (OCV) of 1.44 V and holds the voltage for 24 h without negligible changes, relatively higher than Pt/C-RuO$_2$ air-cathode based QSS-R-ZAB (OCV ~1.36 V). The discharge polarization curves for both $Fe_{0.33}Sn_{0.67}OSe$ and Pt/C-RuO$_2$ air-cathode based QSS-R-ZABs are displayed in Fig. 6b. The QSS-R-ZAB has a peak power density of ~153.96 mW cm^{-2} at the current density of 261 mA cm^{-2}, which is relatively higher than that of the benchmark Pt/C-RuO$_2$ air-cathode based QSS-R-ZAB (~133.35 mW cm^{-2} at current density of 223 mA cm^{-2}) and superior to that of state-of-the-art air-cathodes based ZABs in literature (Fig. 6b,c and Table S5). When repeated charge−discharge cycling stability with 30 min period per cycle at a fixed current density with 10 mA cm^{-2}, the QSS-R-ZAB maintained the voltage gap of ~0.850 V, it increased slightly from 0.854 V after 55 h, and 0.861 V after 400 h. Whereas the QSS-R-ZABs of Pt/C-RuO$_2$//Zn dropped the voltage gap after 57 h, demonstrating that the $Fe_{0.33}Sn_{0.67}OSe$ maintain excellent cycle life for an air-cathode based QSS-R-ZAB (Figs. 6d, S29) and of reported ZABs in the literature (Table S5), indicating that the $Fe_{0.33}Sn_{0.67}OSe$ air-cathode holds tremendous rechargeability. Moreover, the QSS-R-ZAB exhibited long-term durability over 300 h, even at a higher current density of 20 mA cm^{-2} (Fig. S30), reflecting its great practical applicability. As shown in (Fig. 6e), the QSS-R-ZAB delivered a highest specific capacity of ~656.60 mA h g$_{zn}^{-1}$ at a current density of 10 mA cm^{-2}, outstanding performance than that of the Pt/C-RuO$_2$ air-cathode based QSS-R-ZAB (~594.25 mA h g$_{zn}^{-1}$ at a current density of 10 mA h g$_{zn}^{-1}$). The successfully glowing 51 red LEDs was effectively powered a continuously counted over 10 h with two cells connected QSS-R-ZABs in series, demonstrating its practical utilization (inset of Fig. 6e, Movie S1). To further evaluate these practical aspects towards portable and flexible electronics system, the highly flexible nature of the QSS-ZAB as further examined by cycling repeated the different bending of 0º, 90º, 180º, and − 180º for each angle for 2 h, and there was no noticeable change was observed in both charging and discharging potentials (Fig. 6f), demonstrating that our QSS-R-ZAB could be a promising candidate for flexible electronics. The series connected QSS-R-ZABs with different bending angles power 51 red LEDs without any decay after 1 h (Fig. S31), further proves the excellent flexible nature. The $Fe_{0.33}Sn_{0.67}OSe||Fe_{0.33}Sn_{0.67}OSe$ water electrolyzers powered by a series connected QSS-R-ZABs

and generate H_2 and O_2 continuously, representing a self-driven water splitting system by newly developed $Fe_{0.33}Sn_{0.67}OSe$ based QSS-R-ZABs (Movie S2). The $Fe_{0.33}Sn_{0.67}OSe$ air-cathode in QSS-R-ZABs has outstanding electrochemical stability, the catalysts have further exemplified by TEM and XPS analyses. The TEM images clearly indicates that the $Fe_{0.33}Sn_{0.67}OSe$ nanosheets holds their original structure and crystalline nature without any loss, demonstrating its outstanding electrochemical stability. The high-resolution XPS clearly indicates that the intensity of the Fe 2p, Sn 3d, O 1s, and Se 3d were almost retained without major loss, further indicating the exceptional stability. Therefore, we conclude that the $Fe_{0.33}Sn_{0.67}OSe$ could be a potential candidate to replace standard Pt/C and RuO$_2$ catalysts in overall water splitting and rechargeable QSS-R-ZABs.

Supplementary material related to this article can be found online at doi:10.1016/j.apcatb.2021.120924.

Such superior multifunctional ORR, OER, and HER performance could be ascribed to the following aspects: (1) Hierarchical 3D nano-architectures with larger electroactive surface areas could help to improve the ion transport kinetics. Concurrently, oxygen enrichment throughout the ultrathin nanosheet arrays could increase the electroactive sites and boost the multifunctional activities. (2) Highly porous Ni foam substrate with high coupling interaction of active materials could simplify the electron transport kinetics and ensuing lower R$_{ct}$. (3) The unique porous features reduce the "dead volume" and boost the mass transport properties to enhance multifunctional ORR, OER, and HER activities. These consequences reveal that the newly developed hierarchical 3D $Fe_{0.33}Sn_{0.67}OSe$ nanosheets are a freestanding multifunctional catalyst for future energy conversion and storage technologies.

4. Conclusion

In summary, we have established a novel strategy to rational design of $Fe_xSn_{1-x}OSe$ nanostructures by a two-step growth−selenization process. The hierarchical 3D $Fe_xSn_{1-x}OSe$ nanostructures employed freestanding, multifunctional OER, HER, and ORR activities for overall water electrolyzers and rechargeable QSS-R-ZABs. The superior multifunctional ORR, OER, and HER activities of the optimal $Fe_{0.33}Sn_{0.67}OSe$ catalyst have the following aspects have allocated. First, the phases in the $Fe_{0.33}Sn_{0.67}OSe$ catalyst enriched by oxygen vacancies reveal highly efficient activities especially in oxygen involving ORR and OER performances. Second, hierarchical 3D nanostructures with highly exposed electroactive sites and unique porous networks enhance the electrolyte ion penetration and simplifies mass transport kinetics. Third, the effective doping of the Fe into the SnOSe with perfect electronic structure could improve the synergist interaction between Fe, Sn, and oxyselenide, which also boosts the multifunctional catalytic activities. The $Fe_{0.33}Sn_{0.67}OSe$ superior catalyst exhibits multifunctional activities toward ORR (E$_{on}$ ~0.77 V; E$_{1/2}$ ~0.82 V), OER (overpotential of ~162 mV at a current density of 10 mA cm^{-2}), and HER (overpotential of ~61 mV at a current density of 10 mA cm^{-2}), outperforms than that of the conventional Pt/C and RuO$_2$ catalysts. The assembled water electrolyzer realized a cell voltage of 1.49 V at 10 mA cm^{-2}, better than that of Pt/C||RuO$_2$ electrolyzer (~1.545 V) and recently reported water electrolyzer catalysts. Most extraordinarily, rechargeable QSS-R-ZAB cell with high open circuit voltage of 1.44 V, the highest power density of ~153.5 mW cm^{-2}, and also an outstanding life cycle of over 400 h. Furthermore, the rechargeable QSS-R-ZAB demonstrated a good mechanical durability of 10 h under different bending circumstances. In specific, the device connected in series of rechargeable QSS-R-ZABs successfully driven overall water splitting process, demonstrated advanced clean fuel of H_2 gas produced from chemical energy for renewable energy conversion system. We anticipated that this study will opens new prospects for the development of durable and highly active multifunctional catalysts via a facile and cost-effective strategy.

CRediT authorship contribution statement

Mr. Kempanna Harish: He wrote the manuscript and did experiments. **Dr. Jayaraman Balamurugan:** He wrote the manuscript and did the analysis. **Dr. Thanh Tuan Nguyen:** He wrote the manuscript and did the analysis. **Prof Nam Hoon Kim:** He advised the experiments and wrote the manuscript. **Prof Joong Hee Lee:** He advised the experiments and wrote the manuscript.

Declaration of Competing Interest

The authors declare that they have no known competing financial interests or personal relationships that could have appeared to influence the work reported in this paper.

Acknowledgements

Appendix A. Supporting information

Supplementary data associated with this article can be found in the online version at doi:10.1016/j.apcatb.2021.120924.

References

[1] B. Zhang, X. Zheng, O. Voznyy, R. Comin, M. Bajdich, M. García-Melchor, L. Han, J. Xu, M. Liu, L. Zheng, F.P. García de Arquer, C.T. Dinh, F. Fan, M. Yuan, E. Yassitepe, N. Chen, T. Regier, P. Liu, Y. Li, P. De Luna, A. Janmohamed, H.L. Xin, H. Yang, A. Vojvodic, E.H. Sargent, Homogeneously dispersed multimetal oxygen-evolving catalysts, Science 352 (2016) 333–337, https://doi.org/10.1126/science.aaf1525.

[2] D. Aurbach, B.D. McCloskey, L.F. Nazar, P.G. Bruce, Advances in understanding mechanisms underpinning lithium–air batteries, Nat. Energy 1 (2016) 16128, https://doi.org/10.1038/nenergy.2016.128.

[3] I. Roger, M.A. Shipman, M.D. Symes, Earth-abundant catalysts for electrochemical and photoelectrochemical water splitting, Nat. Rev. Chem. 1 (2017) 0003, https://doi.org/10.1038/s41570-016-0003.

[4] Z. Yang, C. Zhao, Y. Qu, H. Zhou, F. Zhou, J. Wang, Y. Wu, Y. Li, Trifunctional self-supporting cobalt-embedded carbon nanotube films for ORR, OER, and HER triggered by solid diffusion from bulk metal, Adv. Mater. 31 (2019), 1808043, https://doi.org/10.1002/adma.201808043.

[5] J. Zhang, Y. Liu, C. Sun, P. Xi, S. Peng, D. Gao, D. Xue, Accelerated hydrogen evolution reaction in CoS₂ by transition-metal doping, ACS Energy Lett. 3 (2018) 779–786, https://doi.org/10.1021/acsenergylett.8b00066.

[6] Y. Gorlin, T.F. Jaramillo, A bifunctional nonprecious metal catalyst for oxygen reduction and water oxidation, J. Am. Chem. Soc. 132 (2010) 13612–13614, https://doi.org/10.1021/ja104587v.

[7] Y. Lin, L. He, T. Chen, D. Zhou, L. Wu, X. Hou, C. Zheng, Cost-effective and environmentally friendly synthesis of 3D Ni₂P from scrap nickel for highly efficient hydrogen evolution in both acidic and alkaline media, J. Mater. Chem. A 6 (2018) 4088–4094, https://doi.org/10.1039/C7TA09524D.

[8] J.R. McKone, A.P. Pieterick, H.B. Gray, N.S. Lewis, Hydrogen evolution from Pt/Ru-coated p-Type WSe₂ photocathodes, J. Am. Chem. Soc. 135 (2013) 223–231, https://doi.org/10.1021/ja308581g.

[9] W. Wang, S. Xi, Y. Shao, X. Gao, J. Lin, C. Meng, W. Wang, X. Guo, G. Li, Sub-nanometer-sized iridium species decorated on mesoporous Co₃O₄ for electrocatalytic oxygen evolution, ChemElectroChem 6 (2019) 1846–1852, https://doi.org/10.1002/celc.201801645.

[10] Q. Feng, Z. Zhao, X.-Z. Yuan, H. Li, H. Wang, Oxygen vacancy engineering of yttrium ruthenate pyrochlores as an efficient oxygen catalyst for both proton exchange membrane water electrolyzers and rechargeable zinc-air batteries, Appl. Catal. B 260 (2020) 118176, https://doi.org/10.1016/j.apcatb.2019.118176.

[11] L.-P. Lv, P. Du, P. Liu, X. Li, Y. Wang, Integrating mixed metallic selenides/nitrogen-doped carbon heterostructures in one-dimensional carbon fibers for efficient oxygen reduction electrocatalysis, ACS Sustain. Chem. Eng. 8 (2020) 8391–8401, https://doi.org/10.1021/acssuschemeng.0c02572.

[12] T. Wang, G. Nam, Y. Jin, X. Wang, P. Ren, M.G. Kim, J. Liang, X. Wen, H. Jang, J. Han, Y. Huang, Q. Li, J. Cho, NiFe (Oxy) hydroxides derived from NiFe disulfides as an efficient oxygen evolution catalyst for rechargeable zn–air batteries: the effect of surface S residues, Adv. Mater. 30 (2018), 1800757, https://doi.org/10.1002/adma.201800757.

[13] J. Zhang, L. Dai, Nitrogen, phosphorus, and fluorine tri-doped graphene as a multifunctional catalyst for self-powered electrochemical water splitting, Angew. Chem. Int. Ed. 55 (2016) 13296–13300, https://doi.org/10.1002/anie.201607405.

[14] J. Wu, R. Zhao, H. Xiang, C. Yang, W. Zhong, C. Zhang, Q. Zhang, X. Li, N. Yang, Exposing highly active (100) facet on a SnS₂/SnO₂ electrocatalyst to boost efficient hydrogen evolution, Appl. Catal. B 292 (2021), 120200, https://doi.org/10.1016/j.apcatb.2021.120200.

[15] R. Wang, Y. Lyu, S. Du, S. Zhao, H. Li, L. Tao, J. Zheng, S. Wang, Defect repair of tin selenide photocathode via in situ selenization: enhanced photoelectrochemical performance and environmental stability, J. Mater. Chem. A 8 (2020) 5342–5349, https://doi.org/10.1039/c9ta13288k.

[16] H. Zhang, M. Zhao, H. Liu, S. Shi, Z. Wang, B. Zhang, L. Song, J. Shang, Y. Yang, C. Ma, L. Zheng, Y. Han, W. Huang, Ultrastable FeCo bifunctional electrocatalyst on Se-doped CNTs for liquid and flexible all-solid-state rechargeable Zn–air batteries, Nano Lett. 21 (2021) 2255–2264, https://doi.org/10.1021/acs.nanolett.1c00077.

[17] M. Fang, G. Dong, R. Wei, J.C. Ho, Hierarchical nanostructures: design for sustainable water splitting, Adv. Energy Mater. 7 (2017), 1700559, https://doi.org/10.1002/aenm.201700559.

[18] J. Yin, Y. Li, F. Lv, M. Lu, K. Sun, W. Wang, L. Wang, F. Cheng, Y. Li, P. Xi, S. Guo, Oxygen vacancies dominated NiS₂/CoS₂ interface porous nanowires for portable Zn–air batteries driven water splitting devices, Adv. Mater. 29 (2017), 1704681, https://doi.org/10.1002/adma.201704681.

[19] T.T. Nguyen, J. Balamurugan, K.-T. Lau, N.H. Kim, J.H. Lee, Novel cobalt-doped molybdenum oxynitride quantum dot@N-doped carbon nanosheets with abundant oxygen vacancies for long-life rechargeable zinc–air batteries, J. Mater. Chem. A 9 (2021) 9092–9104, https://doi.org/10.1039/D0TA12414A.

[20] M.-Q. Yang, J. Wang, H. Wu, G.W. Ho, Noble metal-free nanocatalysts with vacancies for electrochemical water splitting, Small 14 (2018), 1703323, https://doi.org/10.1002/smll.201703323.

[21] X. Gong, J. Zhu, J. Li, R. Gao, Q. Zhou, Z. Zhang, H. Dou, L. Zhao, X. Sui, J. Cai, Self-templated hierarchically porous carbon nanorods embedded with atomic Fe-N4 active sites as efficient oxygen reduction electrocatalysts in Zn-air batteries, Adv. Funct. Mater. 31 (2021), 2008085, https://doi.org/10.1002/adfm.202008085.

[22] Q. Che, Q. Li, Y. Tan, X. Chen, X. Xu, Y. Chen, One-step controllable synthesis of amorphous (Ni-Fe)Sₓ/NiFe(OH)y hollow microtube/sphere films as superior bifunctional electrocatalysts for quasi-industrial water splitting at large-current-density, Appl. Catal. B 246 (2019) 337–348, https://doi.org/10.1016/j.apcatb.2019.01.082.

[23] J. Balamurugan, T.T. Nguyen, D.H. Kim, N.H. Kim, J.H. Lee, 3D nickel molybdenum oxyselenide (Ni₁₋ₓMoₓOSe) nanoarchitectures as advanced multifunctional catalyst for Zn-air batteries and water splitting, Appl. Catal. B 286 (2021), 119909, https://doi.org/10.1016/j.apcatb.2021.119909.

[24] X. Chen, Y. Qiu, G. Liu, W. Zheng, W. Feng, F. Gao, W. Cao, Y. Fu, W. Hu, P. Hu, Tuning electrochemical catalytic activity of defective 2D terrace MoSe₂ heterogeneous catalyst via cobalt doping, J. Mater. Chem. A 5 (2017) 11357–11363, https://doi.org/10.1039/C7TA02327H.

[25] Q. Wu, M. Zhu, J. Cao, X. Wang, Y. Liu, C. Xiang, M. Shao, H. Tian, Z. Kang, Metal-free catalyst with large carbon defects for efficient direct overall water splitting in air at room pressure, ACS Appl. Mater. Interface 12 (2020) 30280–30288, https://doi.org/10.1021/acsami.0c02544.

[26] S.Y. Tee, K.Y. Win, W.S. Teo, L.-D. Koh, S. Liu, C.P. Teng, M.-Y. Han, Recent progress in energy-driven water splitting, Adv. Sci. 4 (2017), 1600337, https://doi.org/10.1002/advs.201600337.

[27] J. Balamurugan, T.T. Nguyen, N.H. Kim, D.H. Kim, J.H. Lee, Novel core-shell CuMo-oxynitride@N-doped graphene nanohybrid as multifunctional catalysts for rechargeable zinc-air batteries and water splitting, Nano Energy 85 (2021), 105987, https://doi.org/10.1016/j.nanoen.2021.105987.

[28] Q. Liu, Y. Wang, L. Dai, J. Yao, Scalable fabrication of nanoporous carbon fiber films as bifunctional catalytic electrodes for flexible Zn-Air batteries, Adv. Mater. 28 (2016) 3000–3006, https://doi.org/10.1002/adma.201506112.

[29] Q. Shi, Q. Liu, Y. Ma, Z. Fang, Z. Liang, G. Shao, B. Tang, W. Yang, L. Qin, X. Fang, High-performance trifunctional electrocatalysts based on FeCo/Co₂P hybrid nanoparticles for zinc–air battery and self-powered overall water splitting, Adv. Energy Mater. 10 (2020) 1903854, https://doi.org/10.1002/aenm.201903854.

[30] W. Shi, M. Gao, J. Wei, J. Gao, C. Fan, E. Ashalley, H. Li, Z. Wang, Tin selenide (SnSe): growth, properties, and applications, Adv. Sci. 5 (2018), 1700602, https://doi.org/10.1002/advs.201700602.

[31] Y.K. Lee, Z. Luo, S.P. Cho, M.G. Kanatzidis, I. Chung, Surface oxide removal for polycrystalline snse reveals near-single-crystal thermoelectric performance, Joule 3 (2019) 719–731, https://doi.org/10.1016/j.joule.2019.01.001.

[32] C. Di Valentin, G. Pacchioni, A. Selloni, Origin of the different photoactivity of N-doped anatase and rutile TiO₂, Phys. Rev. B 70 (2004), 085116, https://doi.org/10.1103/PhysRevB.70.085116.

[33] T.T. Nguyen, J. Balamurugan, V. Aravindan, N.H. Kim, J.H. Lee, Boosting the energy density of flexible solid-state supercapacitors via both ternary NiV₂Se₄ and NiFe₂Se₄ nanosheet arrays, Chem. Mater. 31 (2019) 4490–4504, https://doi.org/10.1021/acs.chemmater.9b01101.

[34] X. Zhong, Y. Feng, W. Knoll, M. Han, Alloyed ZnₓCd₁₋ₓS nanocrystals with highly narrow luminescence spectral width, J. Am. Chem. Soc. 125 (2003) 13559–13563, https://doi.org/10.1021/ja036683a.

[35] L. Vegard, Die Konstitution der Mischkristalle und die Raumfüllung der Atome, Z. Phys. 5 (1921) 17, https://doi.org/10.1007/bf01349680.

[36] R. Shannon, Revised effective ionic radii and systematic studies of interatomic distances in halides and chalcogenides, Acta Crystallogr. Sect. A 32 (1976) 751–767, https://doi.org/10.1107/S0567739476001551.

[37] Y. Guo, C. Zhang, J. Zhang, K. Dastafkan, K. Wang, C. Zhao, Z. Shi, Metal–organic framework-derived bimetallic nife selenide electrocatalysts with multiple phases for efficient oxygen evolution reaction, ACS Sustain. Chem. Eng. 9 (2021) 2047–2056, https://doi.org/10.1021/acssuschemeng.0c06969.

[38] R. Balaji, J. Balamurugan, T.T. Nguyen, N.H. Kim, J.H. Lee, Tunable construction of $Fe_xCo_{3-x}Se_4$ nanostructures as advanced electrode for boosting capacity and energy density, Chem. Eng. J. 390 (2020), 124557, https://doi.org/10.1016/j.cej.2020.124557.

[39] X. Zheng, X. Han, Y. Cao, Y. Zhang, D. Nordlund, J. Wang, S. Chou, H. Liu, L. Li, C. Zhong, Y. Deng, W. Hu, Identifying dense $NiSe_2/CoSe_2$ heterointerfaces coupled with surface high-valence bimetallic sites for synergistically enhanced oxygen electrocatalysis, Adv. Mater. 32 (2020), 2000607, https://doi.org/10.1002/adma.202000607.

[40] Y.-J. Tang, Y. Wang, K. Zhou, In situ oxidation transformation of trimetallic selenide to amorphous FeCo-oxyhydroxide by self-sacrificing $MoSe_2$ for efficient water oxidation, J. Mater. Chem. A 8 (2020) 7925–7934, https://doi.org/10.1039/C9TA14133B.

[41] Y. Liang, Y. Li, H. Wang, J. Zhou, J. Wang, T. Regier, H. Dai, Co_3O_4 nanocrystals on graphene as a synergistic catalyst for oxygen reduction reaction, Nat. Mater. 10 (2011) 780–786, https://doi.org/10.1038/nmat3087.

[42] D. Yan, Y. Li, J. Huo, R. Chen, L. Dai, S. Wang, Defect chemistry of nonprecious-metal electrocatalysts for oxygen reactions, Adv. Mater. 29 (2017), 1606459, https://doi.org/10.1002/adma.201606459.

[43] M. Kuang, Q. Wang, H. Ge, P. Han, Z. Gu, A.M. Al-Enizi, G. Zheng, $CuCoO_x/FeOOH$ core–shell nanowires as an efficient bifunctional oxygen evolution and reduction catalyst, ACS Energy Lett. 2 (2017) 2498–2505, https://doi.org/10.1021/acsenergylett.7b00835.

[44] G. Jiang, H. Zhu, X. Zhang, B. Shen, L. Wu, S. Zhang, G. Lu, Z. Wu, S. Sun, Core/shell face-centered tetragonal FePd/Pd nanoparticles as an efficient non-Pt catalyst for the oxygen reduction reaction, ACS Nano 9 (2015) 11014–11022, https://doi.org/10.1021/acsnano.5b04361.

[45] S. Liu, M. Wang, X. Sun, N. Xu, J. Liu, Y. Wang, T. Qian, C. Yan, Facilitated oxygen chemisorption in heteroatom-doped carbon for improved oxygen reaction activity in all-solid-state zinc–air batteries, Adv. Mater. 30 (2018), 1704898, https://doi.org/10.1002/adma.201704898.

[46] J. Balamurugan, T.T. Nguyen, V. Aravindan, N.H. Kim, J.H. Lee, Highly reversible water splitting cell building from hierarchical 3D nickel manganese oxyphosphide nanosheets, Nano Energy 69 (2020), 104432, https://doi.org/10.1016/j.nanoen.2019.104432.

[47] Y. Jiao, Y. Zheng, M. Jaroniec, S.Z. Qiao, Design of electrocatalysts for oxygen-and hydrogen-involving energy conversion reactions, Chem. Soc. Rev. 44 (2015) 2060–2086, https://doi.org/10.1039/C4CS00470A.

[48] G. Fu, Y. Chen, Z. Cui, Y. Li, W. Zhou, S. Xin, Y. Tang, J.B. Goodenough, Novel hydrogel-derived bifunctional oxygen electrocatalyst for rechargeable air cathodes, Nano Lett. 16 (2016) 6516–6522, https://doi.org/10.1021/acs.nanolett.6b03133.

[49] T.T. Nguyen, J. Balamurugan, D.H. Kim, N.H. Kim, J.H. Lee, Hierarchical 3D oxygenated cobalt vanadium selenide nanosheets as advanced electrode for flexible zinc–cobalt and zinc–air batteries, Small 16 (2020), 2004661, https://doi.org/10.1002/smll.202004661.

[50] B.H.R. Suryanto, Y. Wang, R.K. Hocking, W. Adamson, C. Zhao, Overall electrochemical splitting of water at the heterogeneous interface of nickel and iron oxide, Nat. Commun. 10 (2019) 5599, https://doi.org/10.1038/s41467-019-13415-8.

[51] Y. Yu, J. Zhou, Z. Sun, Novel 2D transition-metal carbides: ultrahigh performance electrocatalysts for overall water splitting and oxygen reduction, Adv. Funct. Mater. 30 (2020), 2000570, https://doi.org/10.1002/adfm.202000570.